Research Square

Preprints are preliminary reports that have not undergone peer review.
They should not be considered conclusive, used to inform clinical practice,
or referenced by the media as validated information.

Valorization of Popocatépetl volcanic ash as a sustainable photocatalyst for ciprofloxacin removal

Julio César Espinoza-Tapia

julio.espinoza@enp.unam.mx

UNAM: Universidad Nacional Autonoma de Mexico https://orcid.org/0000-0003-4154-1594

Iris Zuen Hernández Hernández

UNAM: Universidad Nacional Autonoma de Mexico

Isaías Hernández–Pérez

UAM: Universidad Autonoma Metropolitana

José Antonio Colín–Luna

UAM: Universidad Autonoma Metropolitana

Leonardo González-Reyes

UAM: Universidad Autonoma Metropolitana

Marco Antonio Polo–Labarrios

UNAM: Universidad Nacional Autonoma de Mexico

Elian Viyeri López Arriaga

UNAM: Universidad Nacional Autonoma de Mexico

Ciro Falcony–Guajardo

CINVESTAV IPN: Centro de Investigacion y de Estudios Avanzados del Instituto Politecnico Nacional

Research Article

Keywords: Antimicrobial resistance, Ciprofloxacin, Heterogeneous photocatalysis, Iron oxide, Volcanic ash valorization, Sustainable water treatment

Posted Date: August 3rd, 2026

DOI: https://doi.org/10.21203/rs.3.rs-10124665/v1

License: This work is licensed under a Creative Commons Attribution 4.0 International License. Read Full License

Abstract

The widespread occurrence of fluoroquinolone antibiotics in surface waters and wastewater effluents is recognized as one of the environmental drivers of antimicrobial resistance (AMR). Ciprofloxacin (CPF), one of the most prescribed fluoroquinolones, is poorly removed by conventional treatment trains and persists in aquatic systems at concentrations ranging from ng L^{-1} to µg L^{-1}. Heterogeneous photocatalysis is among the most studied advanced oxidation processes for CPF removal, but the dominant benchmark commercial TiO_2 P25 is produced by an energy-intensive route whose cost is a barrier to community-scale water remediation in low- and middle-income regions. In this work, we evaluate Popocatépetl volcanic ash, an abundant and recurrent atmospheric residue in central Mexico, as a sustainable iron-bearing photocatalyst for CPF degradation. The material was used as collected (Ash 298) and after thermal treatment at 623 K and 823 K (Ash 623, Ash 823) and was characterized by X-ray diffraction, Raman spectroscopy, UV–Vis diffuse reflectance and SEM/EDS. The three samples consist of an aluminosilicate matrix (quartz, cristobalite, labradorite, muscovite) hosting 40–44 wt % of iron-bearing phases, with hematite (α-Fe_2O_3, 14–17 wt %) unambiguously identified and a secondary iron-bearing phase (SIBP, 25–28 wt%) tentatively present. Effective bandgaps of 3.51–3.52 eV match the emission of commercial UV-A lamps (350–365 nm). Under identical conditions (pH 2, $[CPF]_0$ = 20 mg L^{-1}, 1.25 g L^{-1} catalyst, 180 min), the three ashes removed 53–56% of CPF, with pseudo-first-order constants of 0.0048–0.0052 min^{-1}, outperforming commercial TiO_2 P25 (47%, 0.0039 min^{-1}). After subtracting photolytic (8%) and dark-adsorption (12–15%) contributions, the net photocatalytic removal is 30–35%. Iron-normalized rate constants are 27–39 times higher for the ash than the corresponding titanium-normalized value for P25, indicating an efficient use of the active sites. The untreated Ash 298 sample shows the highest rate constant, which supports its use without thermal pre-treatment and reinforces the sustainability argument. The results support the valorization of Popocatépetl volcanic ash as a low-cost photocatalyst for antibiotic-contaminated water in regions of active volcanism.

1. Introduction

Antimicrobial resistance (AMR) has been identified by the World Health Organization as one of the most pressing public health challenges of the 21st century. The release of antibiotic residues from human consumption, hospital effluents and pharmaceutical industries into the aquatic environment is one of the recognized environmental drivers of AMR through selective pressure on microbial communities (Urban-Chmiel et al. 2022; Kümmerer 2003). Among the antibiotics consumed worldwide, fluoroquinolones have received particular attention because of their high prescription rates, their environmental persistence, and their detection in wastewater treatment plant influents and effluents, hospital effluents and surface waters at concentrations ranging from ng L^{-1} to µg L^{-1}. Ciprofloxacin (CPF), one of the most prescribed broad-spectrum fluoroquinolones, is poorly biodegradable, exhibits considerable sorption onto solids, and is only partially removed by conventional treatment (coagulation, filtration, biological treatment, chlorination), so that residual concentrations sufficient to maintain antimicrobial selective pressure regularly reach receiving water bodies.

Advanced oxidation processes (AOPs) are among the most studied technologies for the removal of CPF and related contaminants of emerging concern. Among AOPs, heterogeneous photocatalysis using semiconductor materials under ultraviolet (UV) or visible irradiation has been intensively investigated (Hernández-Ramírez and Medina-Ramírez 2015; Ocampo et al. 2018). The dominant benchmark for heterogeneous photocatalysis is commercial anatase TiO_2 P25 (bandgap ≈ 3.2 eV), which is produced by a flame-hydrolysis route that is energy-intensive and proprietary. Although P25 is the de facto reference material for laboratory studies, its current market price (per kg of treated water in scaled-up operation) is a significant barrier to its deployment for community-scale water remediation in low- and middle-income regions. There is, therefore, an explicit demand for *alternative photocatalysts based on abundant, locally available, naturally occurring or waste-derived materials*, a demand that aligns with United Nations Sustainable Development Goals 6 (clean water and sanitation) and 12 (responsible production and consumption).

Iron oxides are intrinsically attractive in this context. Hematite (α-Fe_2O_3) has a bandgap of 2.1–2.3 eV, absorbs a fraction of the visible region, is chemically stable, non-toxic, and orders of magnitude cheaper than TiO_2 (Mishra and Chun 2015; Tamirat et al. 2016; Garibay Febles et al. 2022). Surface iron sites can participate in redox cycles that generate hydroxyl radicals under irradiation, including at near-neutral pH when iron is properly dispersed on a high-surface-area matrix (Pignatello et al. 2006; Nidheesh 2015; Orozco et al. 2008). The combination of an iron oxide active phase with a high-area aluminosilicate support is therefore a logical design for a low-cost photocatalyst.

Volcanic ash from explosive eruptions of intermediate composition consistently contains hematite and other iron-bearing phases dispersed in an aluminosilicate matrix (Borges et al. 2008; Esparza et al. 2010). The Popocatépetl volcano in central Mexico has been in a state of recurrent low- to moderate-intensity activity for more than three decades, depositing thousands of tonnes of ash per year over the metropolitan area of Mexico City and surrounding states (Siebe and Macías 2006; Martin Del Pozzo et al. 2008). At present this material is mostly treated as an environmental nuisance and a respiratory-health concern (Damby et al. 2014; Horwell et al. 2003), and only limited efforts have been directed at its valorization. Borges and co-workers have shown that volcanic ash from the Canary Islands can degrade phenols and synthetic dyes under solar irradiation (Borges et al. 2016), but, to the best of our knowledge, *the use of Popocatépetl volcanic ash for the removal of fluoroquinolone antibiotics, and specifically for CPF, has not been reported.*

In the present work we hypothesize that volcanic ash from Popocatépetl, with its iron-bearing phases dispersed in an aluminosilicate matrix, can act as an effective photocatalyst for CPF degradation under UV-A irradiation. The specific objectives are: (i) to characterize mineralogically, optically and morphologically the volcanic ash both as collected and after thermal treatment at 623 K and 823 K; (ii) to evaluate the photocatalytic activity towards CPF and to benchmark it against commercial TiO_2 P25 under identical conditions; (iii) to discriminate the relative contributions of direct photolysis, dark adsorption and photocatalysis to the overall CPF removal; (iv) to fit the degradation data to a pseudo-first-order kinetic model, to derive initial rates, half-lives and iron-normalized rate constants, and to

discuss the influence of the iron-bearing fraction on photocatalytic performance; and (v) to discuss the practical implications and current operational limitations of valorizing volcanic ash for the treatment of antibiotic-contaminated water in volcanic regions of the Global South.

2. Materials and methods

2.1 Materials and thermal treatment

Volcanic ash was collected from atmospheric deposition of recurrent exhalations of the Popocatépetl volcano in central Mexico. The as-collected material was air-dried and sieved through a 200-mesh screen (74 μm). Three sub-samples were used: an untreated reference, and two thermally treated portions. Thermal treatments were carried out in a muffle furnace at 623 K and 823 K for 360 min with a heating ramp of 5°C min^{-1} and natural cooling. The three samples are denoted *Ash 298*, *Ash 623* and *Ash 823* according to their treatment temperature. Commercial TiO_2 P25 (Evonik Industries, anatase/rutile ≈ 80/20) was used without further treatment as a benchmark photocatalyst. Ciprofloxacin (CPF, Sigma-Aldrich, ≥ 98% purity), hydrochloric acid (HCl 0.5 M Sigma-Aldrich) and ultrapure water (Milli-Q, 18.2 MΩ cm) were used as received.

2.2 Characterization

X-ray diffraction (XRD) patterns were recorded on a Bruker D8 diffractometer using Cu-Kα radiation (λ = 0.15406 nm) operated at 35 kV and 20 mA, with a step size of 0.02° and a counting time of 1 s per step over the range 10–70° (2θ). Phase identification was carried out by the Hanawalt method using the X'Pert HighScore Plus 3.0 software and the PDF-2 database. Semi-quantitative phase composition was estimated by the integrated areas method; values reported in Table 1 should be regarded as approximations and the relative trends between samples are emphasized over the absolute values.

Raman spectra were recorded on a BWTEK BAC 151i-plus spectrometer using a 532 nm laser at 80% power, with 15 accumulations per measurement, over the range 100–1000 cm^{-1}. Baseline correction was performed before Lorentzian fitting of the bands of interest.

UV–Vis diffuse reflectance spectroscopy (UV–Vis DRS) was carried out on a Varian Cary I spectrophotometer equipped with an integrating sphere using MgO as a reflectance standard. The reflectance data were converted to the Kubelka–Munk function $F(R_\infty) = (1 - R_\infty)^2/2R_\infty$ (Kubelka and Munk 1931; Jubu et al. 2020). Effective bandgap energies (E_g) were estimated using the Tauc method for a direct allowed transition, by extrapolating the linear region of $[F(R_\infty)hv]^2$ versus hv.

Morphology and elemental composition were examined on a JEOL JSM-6701F field-emission scanning electron microscope (SEM) operated at 15 kV, equipped with a secondary-electron detector (SEI) and an energy-dispersive X-ray spectroscopy (EDS) system. At least five different regions were analyzed per sample and average values with standard deviation are reported (Goldstein et al. 2018; Russ 1984).

2.3 Photodegradation experiments

Photocatalytic experiments were carried out in a batch quartz photoreactor charged with 200 mL of CPF solution at an initial concentration of 20 mg L^{-1}. The pH was adjusted to 2.0 ± 0.1 with 0.5 M HCl, the catalyst loading was 1.25 g L^{-1} (250 mg in 200 mL), and the suspension was kept under magnetic stirring at 350 rpm and 25 ± 1°C using a thermostatic bath. Prior to irradiation, the suspension was equilibrated in the dark for 30 min to reach adsorption equilibrium; the resulting concentration was taken as C_0 for the kinetic analysis. The irradiation source was a 10 W mercury lamp (LUMINACTION ES10BLB) whose emission spectrum was characterized with a StellarNet C-SR-50 spectroradiometer and shows a main peak at 365 nm and a secondary band at 350 nm (Fig. 4).

Aliquots of 4 mL were collected at regular intervals during 180 min, centrifuged at 8000 rpm for 5 min, and the supernatant was analyzed for residual CPF by UV–Vis spectroscopy at 273 nm (Varian Cary I) using a calibration curve in the range 0.5–25 mg L^{-1} (Lambert–Beer, $R^2 > 0.999$). All experiments were performed in triplicate and results are expressed as mean ± standard deviation. Two control experiments were carried out: (i) direct photolysis (UV light, CPF, no catalyst), and (ii) dark adsorption (catalyst, CPF, no light).

3. Results and discussion

3.1 Mineralogy and phase composition

The X-ray diffraction patterns of the three samples (Fig. 1) reveal a complex assemblage of silicate, aluminosilicate and iron-bearing phases that is preserved across the thermal treatment range investigated. The unambiguously identified phases are quartz (Q, PDF 83-2466), cristobalite (C, PDF 82-1405), hematite (H, α-Fe_2O_3, PDF 73–0603), labradorite (L, $Ca_{0.68}Na_{0.3}Al_{1.66}Si_{2.34}O_8$, PDF 83-1372) and muscovite (Mu, $KAl_3Si_3O_{10}(OH)_2$, PDF 75–0948). The overall mineral assembly is consistent with previous reports on the mineralogy of Popocatépetl ash (Siebe and Macías 2006; Martin Del Pozzo et al. 2008) and with the wider literature on andesitic-source volcanic ashes (Borges et al. 2008; Esparza et al. 2010; Damby et al. 2014). The coexistence of cristobalite and quartz in andesitic ashes has been documented in detail by Damby and co-workers (2014) for the 2010 Merapi tephra and by González-Reyes et al. (2026) for Popocatépetl specifically; the diffractograms reported here are in close agreement with those references both in the peak positions of the two SiO_2 polymorphs and in their relative intensity ratios. The simultaneous presence of feldspar (labradorite) and mica (muscovite) phases is also typical of andesitic eruption products of the Trans-Mexican Volcanic Belt (Martin Del Pozzo et al. 2008) and serves as a useful mineralogical fingerprint that distinguishes this material from basalt-derived ashes (which contain little or no plagioclase of labradorite composition) and from rhyolitic ashes (which are dominated by sanidine and rich in volcanic glass).

A second set of reflections in the 22–29° (2θ) region was tentatively indexed to a mackayite-type structure ($Fe(OH)(Te_2O_5)$, PDF 70-1915) on the basis of Hanawalt matching. Two independent observations make this assignment problematic. *First* EDS analysis (Table 4) did not detect tellurium in any of the three samples above the detection limit (≈ 0.1 wt %), which is incompatible with a Te-rich phase present at ≈ 25 wt %. *Second*, the relative intensity of this set of reflections evolves *non-monotonically* with thermal treatment it increases from 25.7 wt% (Ash 298) to 27.9 wt% (Ash 623) and then decreases to 25.2 wt % (Ash 823) whereas the corresponding Raman band at 638–642 cm^{-1} decreases monotonically in relative intensity with treatment temperature (Section 3.2). This XRD/Raman asymmetry would not be expected for a single, well-defined crystalline phase, in which both responses should evolve in the same direction. It is, however, fully consistent with a *polyphasic Fe-bearing component* whose relative contributions to the XRD and Raman signals depend on different physical cross-sections (X-ray scattering vs. polarizability of the lattice modes) and on different sensitivities to local order. The same reflections are also compatible with magnetite, maghemite (γ-Fe_2O_3) or with hydrated iron-bearing oxides previously reported in andesitic ash (Borges et al. 2008; Esparza et al. 2010). For these reasons, we refer to this contribution as the *secondary iron-bearing phase* (SIBP). The semi-quantitative value reported in Table 1 should therefore be interpreted strictly as the mass attributable to non-hematite Fe-bearing crystallites; a definitive identification by Mössbauer spectroscopy or synchrotron XRD with Rietveld refinement is beyond the scope of the present study and will be addressed in a follow-up work. *We emphasize that the conclusions drawn below for the photocatalytic activity rely only on the well-identified hematite content and on the total surface Fe loading (EDS)*, neither of which depends on the final identity of the SIBP.

Semi-quantitative analysis (Table 1) places the total iron-bearing fraction at 39.9 wt% in Ash 298, 44.4 wt% in Ash 623 and 42.0 wt% in Ash 823. The hematite contribution increases monotonically from 14.2 wt% (Ash 298) to 16.8 wt% (Ash 823), accompanied by a sharpening of the characteristic (012) and (110) reflections at 24.6° and 36.0° (insets in Fig. 1). This indicates a thermally induced recrystallization of hematite and an increase in its average crystallite size, consistent with the literature on iron oxides annealed at intermediate temperatures (Kundu et al. 2024). The silicate phases remain unchanged in identity but display progressively sharper reflections at higher treatment temperatures, signaling the loss of structural water and an increase in crystallinity in the matrix. In particular, the (101) reflection of quartz at 26.6° and the (101) reflection of cristobalite at 21.8° become progressively narrower and more intense between Ash 298 and Ash 823, reflecting the consolidation of the silica matrix already documented in andesitic ashes subjected to comparable thermal cycles (Horwell et al. 2003; Guinebretière 2007; Martin Del Pozzo et al. 2008).

Table 1
Semi-quantitative phase composition (wt %) of the thermally treated volcanic ash samples, determined from XRD integrated peak areas. Values are means ± standard deviation (n = 3 independent measurements). SIBP = secondary iron-bearing phase

Phase	Chemical formula	Ash 298 (%)	Ash 623 (%)	Ash 823 (%)
SIBP	Fe-bearing	25.7 ± 1.2	27.9 ± 1.4	25.2 ± 1.3
Hematite (H)	α-Fe_2O_3	14.2 ± 0.8	16.5 ± 0.9	16.8 ± 1.0
Labradorite (L)	$Ca_{0.68}Na_{0.3}Al_{1.66}Si_{2.34}O_8$	17.9 ± 0.9	18.3 ± 1.1	18.6 ± 1.0
Muscovite (Mu)	$KAl_3Si_3O_{10}(OH)_2$	16.5 ± 0.8	16.8 ± 0.9	17.5 ± 1.1
Cristobalite (C)	SiO_2	17.3 ± 0.9	15.4 ± 0.8	16.8 ± 0.9
Quartz (Q)	SiO_2	8.4 ± 0.5	5.1 ± 0.4	5.1 ± 0.4
Hematite + SIBP	Total Fe-bearing fraction	39.9	44.4	42.0

The quartz fraction decreases from 8.4 wt % (Ash 298) to 5.1 wt% in both Ash 623 and Ash 823, while the cristobalite fraction varies non-monotonically (17.3 → 15.4 → 16.8 wt %); both observations are consistent with a partial quartz → cristobalite re-crystallization pathway at 623 K, followed by stabilization of the silica phase distribution above 800 K. No new crystalline phases were detected after thermal treatment, confirming that the mineral assembly is preserved but with a favorable redistribution of the iron-bearing species towards the particle surfaces a structural feature with direct relevance for the photocatalytic activity discussed in Section 3.6.

3.2 Vibrational fingerprint

Raman spectroscopy provides an independent confirmation of the iron-oxide phases identified by XRD and, more importantly, a quantitative probe of the local structural order of the hematite component. The spectra of the three samples (Fig. 2) display the five characteristic bands of hematite at ≈ 225, 245, 292, 410 and 612 cm^{-1}, which correspond to the A_{1g} and E_g phonon modes of the corundum-type structure (Shim and Duffy 2002; de Faria et al. 1997; Ravindran et al. 2011). A weaker band between 638 and 642 cm^{-1} is attributable to the SIBP (Shebanova and Lazor 2003; Hanesch 2009). The five hematite bands are present in all three samples with negligible shifts in their central positions (Table 2), confirming that the corundum-type structure is preserved across the thermal treatment range and that the chemical identity of the dominant iron-oxide phase does not change with thermal treatment.

What does change systematically with thermal treatment is the *band width*, which encodes information about average crystallite size and structural disorder. Qualitatively, the hematite bands in Ash 298 particularly the prominent E_g mode at 292 cm^{-1} and the A_{1g} mode at 612 cm^{-1} are visibly broader than the corresponding bands in Ash 623 and Ash 823, and the full width at half maximum (FWHM) values obtained from Lorentzian fitting decrease monotonically with treatment temperature (qualitative

observation; explicit FWHM values are not tabulated here because overlapping silicate contributions in the 200–300 cm^{-1} region complicate baseline subtraction for two of the five hematite bands). The observed narrowing has two physical contributions that operate in the same direction: (i) an *increase in average crystallite size*, which reduces the phonon-confinement contribution to band broadening (smaller crystallites relax the $q \approx 0$ selection rule and broaden the Raman bands), and (ii) a *decrease in the density of point defects, oxygen vacancies and lattice strain* in the hematite, which reduces the inhomogeneous broadening of the phonon modes. Both effects are well established in the Raman literature on iron oxides (Jubb and Allen 2010) and are consistent with the XRD evidence of peak sharpening in the (012) and (110) hematite reflections at higher temperatures (Section 3.1).

This monotonic band-narrowing trend has direct implications for the photocatalytic activity. Hematite exhibits a non-trivial dependence of photocatalytic performance on crystallite size: extremely small crystallites suffer from charge recombination at extended defects, while extremely large and highly crystalline hematite particles lose surface-site density and reactive defect concentration (Almeida et al. 2009; Marelli et al. 2014). The broader Raman bands in Ash 298 therefore signal a higher density of catalytically active defect sites and a smaller average crystallite size compared with the thermally treated samples a feature that, as discussed in Section 3.6, correlates with the highest pseudo-first-order rate constant observed in this study. Conversely, the narrowest bands in Ash 823 signal the most crystalline (i.e. most extensively annealed) hematite, whose lower defect density does *not* translate into improved performance. The Raman evidence therefore directly supports the conclusion that an *intermediate level of structural disorder*, rather than maximum crystallinity, is the optimal state of the iron-bearing phase for this reaction.

The SIBP band at 638–642 cm^{-1} decreases in relative intensity from Ash 298 to Ash 823 and shifts very slightly to higher wavenumbers with thermal treatment (Table 2). This evolution is consistent with the partial thermal decomposition of hydrated/secondary iron-bearing phases and with their progressive transformation into more stable, less hydrated iron-oxide phases at the highest treatment temperatures. Importantly, this Raman trend *differs from* the XRD trend for the same phase (which is non-monotonic, peaking at Ash 623; see Section 3.1), reinforcing the conclusion that the SIBP is not a single, well-defined crystalline component but rather a polyphasic Fe-bearing contribution whose XRD scattering and Raman polarizability respond differently to thermal evolution. This XRD/Raman asymmetry is a further reason for the conservative SIBP designation adopted in this work.

Table 2
Raman peak positions (cm^{-1}) and vibrational mode assignments for the thermally treated volcanic ash samples. Peaks 1–5 correspond to hematite; peak 6 corresponds to the secondary iron-bearing phase (SIBP).

Sample	Peak 1	Peak 2	Peak 3	Peak 4	Peak 5	Peak 6 (SIBP)
Ash 298	225.3	245.1	292.6	411.8	612.3	638.5
Ash 623	225.1	245.2	292.5	411.9	612.1	640.2
Ash 823	224.8	245.0	292.4	411.5	612.0	642.0

3.3 Optical properties

The effective optical bandgaps obtained from UV-Vis DRS via the Kubelka-Munk function and Tauc analysis are 3.52, 3.51 and 3.51 eV for Ash 298, Ash 623 and Ash 823, respectively (Table 3). These values are markedly higher than the bandgap of pure hematite (2.1–2.3 eV; Gardner et al. 1963; Marelli et al. 2014). The blue shift relative to bulk hematite is consistent with the intimate mixing between the iron-oxide nanoparticles and the wide-gap silicate matrix (E_g > 4 eV), which dominates the effective absorption edge of the composite (Mittal et al. 2015). This observation has two practical consequences. First the absorption onset of the three samples (352–353 nm via the Planck-Einstein relation $\lambda_{exc} = hc/E_g$) matches the emission of common UV-A lamps (the lamp used here has its main band at 365 nm and a secondary band at 350 nm, Fig. 4), confirming that the ashes can be activated by inexpensive commercial lamps. Second, *the very small variation in bandgap among the three samples (3.51–3.52 eV) confirms that the differences in photocatalytic activity reported below are not driven by light absorption* and must instead reflect differences in active-site density, surface composition and charge-carrier dynamics.

Table 3
Effective bandgap energies and corresponding threshold excitation wavelengths of the thermally treated volcanic ash samples, determined by the Kubelka-Munk method assuming a direct allowed transition.

Sample	Bandgap E_g (eV)	Excitation λ_{exc} (nm)
Ash 298	3.52	352
Ash 623	3.51	353
Ash 823	3.51	353

3.4 Morphology and surface Composition

Representative SEM micrographs of the three samples are shown in Fig. 3 at two magnifications (×10,000 and ×50,000). The three sample sets display distinct and progressive morphological signatures that, when combined with the surface composition obtained by EDS (Table 4), provide a coherent picture of the thermally driven evolution of the ash.

*Ash 298 (*Fig. 3A–B*).* The as-collected sample exhibits an irregular, predominantly amorphous morphology consisting of agglomerated particles with a heterogeneous size distribution. At low magnification (Fig. 3A), the matrix appears as a continuous grey phase corresponding to the aluminosilicate component (quartz, cristobalite, labradorite and muscovite, as identified by XRD). At ×50,000 magnification (Fig. 3B), brighter sub-micrometric particles of average size ≈ 700 nm are observed (indicated by arrows), embedded within or partially exposed on the silicate matrix. The brighter contrast of these particles is consistent with the higher mean atomic number of iron-bearing phases (hematite and SIBP) compared to the silicate matrix (Faivre and Frankel 2016). EDS analysis (Table 4) of the as-collected sample yields high contents of oxygen (56.27 wt %), silicon (23.68 wt %) and aluminium (14.67 wt %), consistent with a hydroxylated aluminosilicate matrix. Iron accounts for only 2.07 wt%, which sets the baseline surface Fe loading for this study. Minor amounts of Na (1.07 wt %), K (0.67 wt %) and Ca (0.66 wt %) are also detected, corresponding to the feldspar (labradorite) and mica (muscovite) phases (Anthony et al. 1990).

*Ash 623 (*Fig. 3C–D*).* After thermal treatment at 623 K, the morphology shows significant changes. At low magnification (Fig. 3C), the silicate matrix is more compact, with smoother and more cohesive surfaces, which is indicative of partial sintering and of the loss of structural water from the aluminosilicate phases (Guinebretière 2007). At ×50,000 magnification (Fig. 3D), the iron-rich particles appear more numerous and slightly larger, with an average size of ≈ 800 nm, and more importantly they show a more homogeneous distribution on the silica surface than in Ash 298. This more even dispersion is beneficial for photocatalytic activity because it increases the density of accessible Fe-bearing sites per unit area of the matrix (Rajalaxmi and Rajagopala 2001). EDS data (Table 4) reveal a substantial decrease in oxygen (44.69 wt %) and an even more pronounced decrease in aluminum (7.35 wt%) relative to Ash 298. The silicon content rises to 38.95 wt %, reflecting the consolidation of quartz and cristobalite and the relative enrichment of the surface in Si as the lighter atoms (O, H from –OH groups, structural water) are lost. The iron surface content remains essentially unchanged (2.15 wt %), but its dispersion is substantially improved, in agreement with the SEM contrast and with the photocatalytic results reported below.

*Ash 823 (*Fig. 3E–F*).* The highest treatment temperature leads to further morphological evolution. The low-magnification image (Fig. 3E) shows that the silica matrix is now highly compacted and that the quartz particles exhibit well-defined planar surfaces and angular geometries, with sizes reaching up to ≈ 10 µm a clear signature of the recrystallization and growth of the silica phases under prolonged thermal treatment (Horwell et al. 2003; Martin Del Pozzo et al. 2008). The high-magnification image (Fig. 3F) reveals that the iron-rich particles are visibly smaller (≈ 600 nm) than in Ash 623 and that they appear as fine, well-dispersed crystallites decorating the quartz surfaces. This apparent particle-size reduction is attributed to two combined effects: the thermal decomposition of the hydrated SIBP into smaller, more dispersed hematite crystallites (already suggested by the Raman evolution in Section 3.2), and the migration of Fe-bearing particles from the bulk of the matrix to the consolidated silica surfaces during the recrystallization step (Frost and Dickfos 2009). EDS analysis (Table 4) shows a further decrease in oxygen (32.65 wt %) and a marked increase in silicon (44.17 wt %), confirming the dominance of

crystalline silica phases at the surface. The iron content rises to 2.75 wt %, the highest of the three samples; this Fe surface enrichment, together with the finer particle size and the improved dispersion, results in a higher density of surface-exposed Fe sites per unit area, although as discussed in Section 3.6 the photocatalytic activity does not increase proportionally.

Table 4
Elemental surface composition (wt% and at%) of the thermally treated volcanic ash samples determined by EDS at 15 kV. Values are means ± standard deviation (n = 5 regions). Note the absence of Te in all three samples.

Element	Ash 298 (wt%)	Ash 298 (at%)	Ash 623 (wt%)	Ash 623 (at%)	Ash 823 (wt%)	Ash 823 (at%)
O	56.27 ± 2.1	69.53 ± 1.8	44.69 ± 1.9	59.11 ± 1.7	32.65 ± 1.5	47.01 ± 1.4
Na	1.07 ± 0.2	0.92 ± 0.1	2.88 ± 0.3	2.65 ± 0.2	2.76 ± 0.3	2.76 ± 0.2
Al	14.67 ± 1.0	10.74 ± 0.8	7.35 ± 0.7	5.77 ± 0.5	9.46 ± 0.8	8.08 ± 0.6
Si	23.68 ± 1.5	16.67 ± 1.2	38.95 ± 1.8	29.35 ± 1.5	44.17 ± 2.0	36.22 ± 1.6
K	0.67 ± 0.1	0.34 ± 0.1	3.02 ± 0.3	2.17 ± 0.2	5.10 ± 0.4	3.01 ± 0.3
Ca	0.66 ± 0.1	0.33 ± 0.1	0.96 ± 0.1	0.51 ± 0.1	3.11 ± 0.3	1.79 ± 0.2
Fe	2.07 ± 0.2	0.73 ± 0.1	2.15 ± 0.2	0.44 ± 0.1	2.75 ± 0.3	1.13 ± 0.1
Te	n.d.	n.d.	n.d.	n.d.	n.d.	n.d.

Non-monotonic evolution of aluminum and the dihydroxylation story. The EDS data reveal a *non-monotonic* behavior of the aluminum content (14.67 → 7.35 → 9.46 wt % for Ash 298, Ash 623 and Ash 823, respectively), which deserves explicit discussion. The pronounced drop between Ash 298 and Ash 623 is dominated by the *dihydroxylation of muscovite* that is, the loss of OH groups from $KAl_2(AlSi_3O_{10})(OH)_2$ and by the partial structural collapse of its dioctahedral layered network. The 623 K treatment temperature lies within the well-documented dihydroxylation range of dioctahedral micas (≈ 750–950 K depending on layer charge and chemical composition), where the loss of structural water and the partial breakdown of the layered structure displace Al towards the bulk of the matrix and away from the EDS-sampled surface region. The subsequent *slight increase* from Ash 623 (7.35 wt %) to Ash 823 (9.46 wt %) is not associated with any additional supply of Al (the system is closed) but rather with a redistribution of the dehydroxylated Al within the matrix, plausibly involving the formation of Al-substituted silicates (mullite-type Al_2SiO_5 fragments or alkali-feldspar phases) that bring Al back to the EDS-sampled surface region during the high-temperature recrystallization step. This interpretation is consistent with the parallel evolution of oxygen and silicon: the O content (at%) drops from 69.53 → 59.11 → 47.01 and the Si content (at %) rises from 16.67 → 29.35 → 36.22, both of which are consistent with progressive depletion of –OH groups and structural water and with parallel enrichment in covalently bonded Si–O–Si and Si–O–Al networks. The Si/Al atomic ratio increases sharply from 1.55 (Ash 298) to 5.09 (Ash 623) and decreases slightly to 4.48 (Ash 823), confirming the same picture. *Importantly for this work, the iron*

*surface content (*Table 4*) is essentially independent of these matrix re-organizations*, which means that the differences in photocatalytic activity reported below cannot be attributed to a depletion or accumulation of Fe at the surface but must instead reflect differences in the structural state of the iron-bearing crystallites themselves a conclusion that is fully consistent with the Raman evidence presented in Section 3.2.

Finally no tellurium signal was detected in any of the three samples above the EDS detection limit (≈ 0.1 wt %), which confirms that the SIBP component identified by XRD (Section 3.1) cannot be a Te-rich phase such as mackayite. This independent observation strengthens the SIBP designation adopted in this work.

3.5 Photocatalytic removal of ciprofloxacin

3.5.1 Lamp emission and irradiation conditions

The emission spectrum of the UV lamp (Fig. 4) exhibits a main peak at 365 nm and a secondary band at 350 nm with ≈ 50% of the main peak intensity, plus minor bands at 406, 437 and 549 nm associated with the mercury discharge. This emission profile is well-matched to the absorption onset of the three ash samples (λ_{exc} = 352–353 nm, Table 3), guaranteeing efficient photon absorption by the iron-bearing phases of the ash and by the anatase fraction of the P25 reference (bandgap ≈ 3.2 eV, λ_{exc} = 387 nm).

3.5.2 Time-resolved degradation profiles and overall removal

Figure 5 shows the time evolution of the relative residual CPF concentration (C/C_0) under UV-A irradiation for the three volcanic ash samples and for the commercial TiO_2 P25 reference. The two control experiments are also indicated. After 180 min, direct photolysis removes only 8% of the CPF, confirming that the molecule is moderately photostable under UV-A and that bulk photolysis is a minor contributor to the overall removal. The dark-adsorption control yields 12–15% removal depending on the sample, attributable to interaction with the silicate matrix and with hydroxylated iron-bearing surfaces. In the presence of UV-A irradiation, CPF removal reaches 56% for Ash 298, 53% for Ash 623 and 54% for Ash 823, all of which exceed the 47% removal achieved by commercial TiO_2 P25 under identical conditions. The benchmark is therefore reproduced and exceeded, providing a direct quantitative argument for the use of the ash in this application.

3.5.3 Pseudo-first-order kinetics, initial rates and half-lives

The CPF degradation data were fitted to the pseudo-first-order Langmuir–Hinshelwood approximation, valid at low pollutant concentrations:

$$ln(C_0/C) = k_{app} \cdot t \quad (1)$$

where k_{app} is the apparent first-order rate constant. Linear fits of $\ln(C_0/C)$ versus t (Fig. 6) yield correlation coefficients $R^2 > 0.98$ for all samples, confirming the validity of the kinetic model. The fitted k_{app} values, together with two derived quantities the initial degradation rate $r_0 = k_{app} \cdot C_0$ and the half-life $t_{1/2} = \ln 2/k_{app}$ are reported in Table 5.

The rate constants follow the order Ash 298 (0.0052 min^{-1}) > Ash 823 (0.0049 min^{-1}) > Ash 623 (0.0048 min^{-1}) > TiO_2 P25 (0.0039 min^{-1}). The corresponding half-lives are 133, 141, 144 and 178 min, indicating that the three ash samples reduce the time required to halve the CPF concentration by 19–25% relative to P25 under identical conditions.

3.5.4 Net photocatalytic contribution and Fe-normalized performance

Two additional analyses of the existing kinetic data clarify the origin of the activity. First, since the overall CPF removal aggregates three independent contributions direct photolysis, dark adsorption, and photocatalysis these can be separated to a first approximation. Subtracting the photolytic (8%) and dark-adsorption (12–15%) contributions from the overall removal yields a *net photocatalytic contribution* of 30–35% for the three ash samples and 24% for P25 (Table 5). Although this subtraction is approximate (it neglects competitive adsorption between CPF and photolysis intermediates), it makes the photocatalytic contribution explicit and directly comparable across samples. The ash photocatalysts again outperform P25 by 6–11 percentage points in the strictly photocatalytic fraction.

Second, the absolute amount of the active metal in suspension differs by more than an order of magnitude between the ash samples and P25 (anatase TiO_2 is ≈ 60 wt % Ti, whereas the ashes contain only 2.07–2.75 wt % Fe by EDS). A fair comparison of the intrinsic activity of the active sites therefore requires normalisation by the mass of active metal in suspension. Using the catalyst loading (1.25 g L^{-1}) and the elemental compositions of Table 4, the mass concentrations of Fe in the ash suspensions are 0.026 g L^{-1} (Ash 298), 0.027 g L^{-1} (Ash 623) and 0.034 g L^{-1} (Ash 823), whereas the mass concentration of Ti in the P25 suspension is 0.75 g L^{-1}. The corresponding metal-normalized first-order rate constants (k_{app}/[M]) are 0.201, 0.179 and 0.142 L g^{-1} min^{-1} for the three ash samples (per gram of Fe) versus 0.0052 L g^{-1} min^{-1} for P25 (per gram of Ti). *On a per-gram-of-active-metal basis, the iron sites in the volcanic ash are 27–39 times more efficient than the titanium sites in commercial P25 under our conditions.* This is, in our view, the most informative comparison between the two materials: it explicitly accounts for the fact that the ash contains only a small fraction of active metal and yet still delivers an absolute kinetic advantage over the benchmark.

Table 5

Photodegradation parameters for the three volcanic ash samples and the commercial TiO_2 P25 reference. $r_0 = k \cdot C_0$ is the initial degradation rate; $t_{1/2}$ is the half-life; η_{total} is the overall removal at 170 min; η_{photo} is the estimated net photocatalytic contribution after subtracting the photolytic (8%) and dark-adsorption (12–15%) contributions; k_{app} is the metal-normalized rate constant

Sample	k_{app} (min^{-1})	R^2	r_0 (mg L^{-1} min^{-1})	$t_{1/2}$ (min)	η_{total} (%)	η_{photo} (%)	$k_{app}/[M]$ (L g^{-1} min^{-1})
Ash 298	0.0052 ± 0.0002	0.991	0.104	133	56.0 ± 1.2	35	0.201
Ash 623	0.0048 ± 0.0002	0.989	0.096	144	53.0 ± 1.1	32	0.179
Ash 823	0.0049 ± 0.0002	0.990	0.098	141	54.0 ± 1.3	33	0.142
TiO_2 P25	0.0039 ± 0.0002	0.985	0.078	178	47.0 ± 1.5	24	0.0052

3.6 Structure-activity relationship

A key observation in Table 5 is that the rate constant *does not* increase monotonically with hematite content, with crystallinity or with surface Fe loading. The untreated sample (Ash 298), which has the lowest hematite content (14.2 wt %), the lowest surface Fe (2.07 wt %) and the broadest hematite Raman bands (i.e. the lowest crystallite size and highest defect density), nevertheless displays the highest rate constant. Conversely Ash 823 with the highest hematite content (16.8 wt %), the most crystalline hematite (narrowest Raman bands) and the highest surface Fe (2.75 wt %) does not deliver the highest activity. This decoupling has two practical implications.

First the data are consistent with a picture in which the photocatalytic activity is governed not by the total mass of hematite but by the *density of defect-related active sites* on the hematite/SIBP nanoparticles. Hematite is well known to display a strong dependence of photocatalytic activity on crystallite size, oxygen vacancy density and surface OH groups (Almeida et al. 2009; Zhang et al. 2014; Marelli et al. 2014). Thermal treatment at 623–823 K simultaneously increases crystallinity (which is beneficial up to a point because it reduces charge-recombination at extended defects) and reduces the density of point defects and surface OH groups (which is detrimental because it removes potential active sites). The slight loss of activity from Ash 298 to Ash 623/823 suggests that the as-collected ash already strikes a near-optimal balance between these two factors and that further thermal annealing offers no advantage for this reaction.

Second this observation has a direct implication for the sustainability case: *the highest activity is obtained without any thermal treatment*, i.e. without the additional energy cost of calcination. This reinforces the practical attractiveness of the as-collected ash as a low-input photocatalyst, since both

the embodied energy of the calcination step and the operational complexity of a thermal pre-treatment can be avoided without sacrificing performance.

3.7 Mechanistic considerations and limitations

Ciprofloxacin speciation and surface charge. In aqueous solution at pH 2, ciprofloxacin exists predominantly in its protonated cationic form (CPF^+), since both protonation sites the carboxylic acid group ($pKa_1 \approx 6.2$) and the secondary amine of the piperazine ring ($pKa_2 \approx 8.6$) are well below their respective pKa values at this pH (Li et al. 2020). The silicate matrix and the iron-bearing surfaces are also positively charged at this pH because the working value lies well below the point of zero charge of hematite ($pH_{pzc} \approx 8.5$) and of quartz/silica ($pH_{pzc} \approx 2–3$) (Tu et al. 2014). The electrostatic interaction between CPF^+ and the catalyst surface is therefore unfavorable at pH 2, which excludes Coulombic attraction as the dominant adsorption mechanism in our experiments.

Adsorption pathway. The non-zero dark adsorption (12–15%) must therefore arise from non-electrostatic specific interactions. Two contributions are plausible. *First*, surface –OH groups on hematite and on the silicate matrix can form hydrogen bonds with the carbonyl, carboxyl and fluorine substituents of ciprofloxacin, allowing for non-electrostatic specific adsorption even on a like-charged surface. *Second*, the piperazine and quinolone rings of CPF can interact with the Fe(III) surface sites via inner-sphere complexation, in which one of the carbonyl oxygens or the carboxylate group of CPF coordinates directly to a surface Fe site. Both interactions are well documented for fluoroquinolones on iron-bearing surfaces at acidic pH (Salma et al. 2016; Hu et al. 2020). The 12–15% dark removal measured in our control experiments is therefore consistent with surface chemisorption rather than bulk physical adsorption, and provides the substrate on which the photocatalytic step can subsequently act.

Photogeneration of electron–hole pairs. Once UV-A irradiation is switched on, the iron-bearing phases of the ash absorb photons with energies above their effective bandgap (3.51–3.52 eV; Section 3.3) and generate electron–hole pairs:

$$\textit{Fe-bearing semiconductor} + h\nu \rightarrow e^-(CB) + h^+(VB) \quad (2)$$

The valence-band hole h^+(VB) has an oxidation potential sufficient to oxidize surface-adsorbed water and surface –OH groups to hydroxyl radicals (·OH):

$$h^+(VB) + H_2O(ads) \rightarrow \cdot OH + H^+ \quad (3)$$

$$h^+(VB) + -OH(surface) \rightarrow \cdot OH \quad (4)$$

In parallel the conduction-band electron e^-(CB) can reduce dissolved O_2 to superoxide radical ($O_2\cdot^-$), which can further evolve to hydroperoxyl ($HO_2\cdot$) and to H_2O_2 in acidic media:

$$e^-(CB) + O_2 \rightarrow O_2\cdot^- \quad (5)$$

$O_2{\cdot}^- + H^+ \rightarrow HO_2{\cdot}$; $2\ HO_2{\cdot} \rightarrow H_2O_2 + O_2$ (6)

Radical attack on the CPF molecule. The hydroxyl radical ·OH is widely accepted as the dominant reactive oxygen species responsible for CPF degradation in heterogeneous photocatalysis (Salma et al. 2016; Hu et al. 2020). Its attack is preferentially directed at the most electron-rich moiety of the CPF molecule, the *piperazine ring*, where the secondary amine and the methylene carbons offer the highest HOMO density and therefore the highest reactivity towards electrophilic radical addition. The reaction is initiated by hydrogen abstraction from a piperazinyl methylene or by direct hydroxyl-radical addition to the C–N bond, followed by sequential oxidation of the secondary amine to an imine, hydrolytic ring-opening of the resulting iminium intermediate, and progressive degradation to lower-molecular-weight aliphatic species. A parallel pathway involves *defluorination* of the aromatic C–F substituent at the C6 position via ·OH attack at the adjacent quinolone carbon, an oxidation step that is energetically less favorable than piperazine attack but kinetically relevant on extended irradiation. These two pathways together account for the bleaching of the CPF absorption band at 273 nm and for the gradual disappearance of the parent compound observed in our experiments (Fig. 5). Full identification of the intermediates by HPLC-MS, and quantification of the degree of mineralization by TOC measurements, were beyond the scope of the present work and will be addressed in a follow-up study.

What can and cannot be claimed from the present dataset. It is important to be explicit about what the present kinetic dataset can and cannot establish regarding the mechanism. We have direct evidence for: (i) photocatalytic activity driven by the iron-bearing phases of the ash, supported by the spectral match between the lamp emission and the effective bandgap, by the bleaching of the CPF chromophore at 273 nm, and by the strong dependence of the rate constant on catalyst composition; (ii) the comparable-or-superior performance of the volcanic ash relative to commercial TiO_2 P25 under strictly identical conditions; and (iii) the dominant role of structural defects rather than total Fe loading, supported by the inverse correlation between hematite crystallinity (Raman/XRD) and apparent rate constant discussed in Section 3.6. We *cannot*, however, claim from the present data alone a heterogeneous photo-Fenton mechanism in the strict sense. Such a claim would require: (a) explicit radical-scavenger experiments using isopropanol for ·OH, EDTA or methanol for h^+, and benzoquinone for $O_2{\cdot}^-$; (b) quantification of the iron leached into solution (by AAS or ICP-MS) and assessment of whether the homogeneous Fenton contribution is significant; and (c) explicit addition of H_2O_2 to the reactor to test whether it enhances the rate constant (a positive signature of Fenton-type contributions). None of these experiments were performed in this work, and the photo-Fenton language has therefore been retained only as a *possible*, rather than established, contribution. The activity is most conservatively described as heterogeneous photocatalysis driven by iron-bearing semiconducting phases, with possible surface-mediated photo-Fenton contributions and the discrimination among these contributions is a defined goal of the follow-up work (Amarzadeh et al. 2023).

Operational limitations. A second operational limitation is the requirement to work at pH 2 in order to prevent precipitation of iron hydroxides and to keep the photocatalyst active. This is a well-recognized drawback of iron-based photocatalysts (Pignatello et al. 2006; Nidheesh 2015), and it is not directly

transferable to the near-neutral pH of real wastewater streams. Strategies to overcome this limitation chelation of iron with organic ligands, supported configurations to minimize leaching, or continuous-flow operation with controlled acidification are an active area of research and a logical next step for the volcanic ash system reported here.

Concentration regime. Finally the initial CPF concentration used in our experiments (20 mg L^{-1}) is several orders of magnitude higher than the environmentally relevant range (ng L^{-1} to µg L^{-1}) and was chosen here to allow reliable UV–Vis quantification via the Lambert–Beer relationship. Although the pseudo-first-order kinetic framework applied here is the low-concentration limit of the Langmuir–Hinshelwood approximation and should remain valid at much lower CPF loads, an experimental validation of the kinetics at the µg L^{-1} scale would require either a pre-concentration step or a more sensitive analytical method (e.g. HPLC-fluorescence or LC-MS), again a logical extension of this work.

4. Conclusions

Popocatépetl volcanic ash, an abundant and recurrent atmospheric residue in central Mexico, has been characterized by XRD, Raman, UV–Vis DRS and SEM/EDS and evaluated as a photocatalyst for the removal of ciprofloxacin under UV-A irradiation. The material consists of an aluminosilicate matrix hosting 40–44 wt % of iron-bearing phases, dominated by hematite (14–17 wt %) and a secondary iron-bearing phase of unresolved identity (25–28 wt%, *not* assigned to a Te-rich mackayite, as initially suggested by Hanawalt matching alone, because no Te was detected by EDS in any sample). The effective bandgap (3.51–3.52 eV) is dominated by the silicate matrix and matches the emission of commercial UV-A lamps, confirming that the material can be activated with inexpensive irradiation sources.

Under standard conditions (pH 2, 20 mg L^{-1} initial CPF, 1.25 g L^{-1} catalyst loading, 180 min UV-A irradiation), the three volcanic ash samples removed 53–56% of the CPF and outperformed commercial TiO_2 P25 (47%) under strictly identical conditions. Pseudo-first-order rate constants of 0.0048–0.0052 min^{-1} for the ashes (vs. 0.0039 min^{-1} for P25) correspond to half-lives of 133–144 min (vs. 178 min). The net photocatalytic contribution, obtained after subtracting the photolytic (8%) and dark-adsorption (12–15%) controls, is 30–35% for the ashes and 24% for P25. When normalized to the mass of active metal in suspension, the iron sites in the ash are 27–39 times more efficient than the titanium sites in P25, providing a quantitative argument for the catalytic relevance of the iron-bearing phases despite their low overall weight fraction.

The highest activity was obtained for the untreated sample (Ash 298), which suggests that the as-collected ash already provides a near-optimal balance between iron-bearing-phase crystallinity, defect density and surface accessibility. Thermal treatment at 623 K or 823 K modestly increased hematite crystallinity but did not improve photocatalytic performance. This finding *reinforces the sustainability argument*: the highest activity is delivered without any energy-consuming thermal pre-treatment, leaving collection, sieving and direct use as the only required processing steps.

Two operational limitations should be acknowledged. First the acidic working pH (2.0) is required to keep iron species reactive and prevent surface fouling and is not directly transferable to real wastewater streams of near-neutral pH; strategies based on chelation, supported configurations or continuous-flow operation are a logical next step. Second, the high initial CPF concentration used here (20 mg L^{-1}) was chosen for analytical reliability and is orders of magnitude higher than environmentally relevant levels. Future work will (i) clarify the relative contributions of heterogeneous photocatalysis and surface photo-Fenton mechanisms through scavenger experiments and iron-leaching measurements; (ii) probe the activity at near-neutral pH using chelation and supported configurations; (iii) identify reaction intermediates by HPLC-MS and assess mineralization by TOC; and (iv) confirm the identity of the secondary iron-bearing phase by Mössbauer spectroscopy. Despite these limitations, the present study demonstrates that abundant Popocatépetl volcanic ash is a chemically robust, mineralogically rich and economically attractive starting material for the design of low-input photocatalysts targeting antibiotic-contaminated water a result with direct relevance for water remediation in volcanic regions of the Global South.

Declarations

Acknowledgements

The authors thank Cinvestav-IPN and Universidad Autónoma Metropolitana-Azcapotzalco for institutional support and access to research infrastructure. The authors are grateful for the technical assistance provided by Rivera Z., Guerrero M., and García Sotelo A. from the Physics Department of Cinvestav-IPN.

Funding

The publication of this article is supported by the Universidad Nacional Autónoma de México (UNAM) through its Transformative Agreement with Springer Nature, administered by the Dirección General de Bibliotecas y Servicios Digitales de Información (DGBSDI).

Author contributions

Julio César Espinoza-Tapia: Conceptualization, methodology, investigation (XRD), supervision, project administration, funding acquisition, writing original draft. *Iris Zuen Hernández Hernández*: Investigation, data curation, formal analysis, validation. *Isaías Hernández-Pérez*: Methodology (design of the photocatalytic system), validation, resources, writing review & editing. *José Antonio Colín-Luna*: Investigation (XRD characterization and phase analysis), formal analysis. *Leonardo González-Reyes*: Investigation (Raman, HRTEM and crystallographic analysis), formal analysis, writing review & editing. *Marco Antonio Polo-Labarrios*: Formal analysis (kinetic modeling), software, visualization. *Elian Viyeri López Arriaga*: Investigation (UV–Vis monitoring, calibration curves), data curation. *Ciro Falcony-*

Guajardo: Resources (access to SEM/EDS and UV–Vis DRS facilities), supervision, writing review & editing, funding acquisition. All authors have read and agreed to the published version of the manuscript.

Ethics approval

This is not applicable

Consent to participate

This is not applicable

Consent to Publish

This is not applicable

Competing Interests

The authors declare no conflict of interest.

Data availability

The raw datasets (XRD patterns, Raman spectra, UV–Vis DRS data, SEM micrographs, EDS spectra, and photodegradation kinetic data) generated and analyzed during the current study are available from the corresponding author on reasonable request.

Mandatory if your study involves humans and/or animals

This is not applicable

References

1. Almeida TP, Fay MW, Zhu Y, Brown PD (2009) Process map for the hydrothermal synthesis of α-Fe_2O_3 nanorods. J Phys Chem C 113:18689–18698. https://doi.org/10.1021/jp907081j
2. Amarzadeh M, Azqandi M, Nateq K, Ramavandi B, Khan NA, Nasseh N. Heterogeneous Fenton-like Photocatalytic Process towards the Eradication of Tetracycline under UV Irradiation: Mechanism Elucidation and Environmental Risk Analysis. Water. 2023; 15(13):2336. https://doi.org/10.3390/w15132336

3. Anthony JW, Bideaux RA, Bladh KW, Nichols MC (1990) Handbook of Mineralogy. Mineral Data Publishing, Tucson, Arizona
4. Borges ME, Álvarez-Galván MC, Esparza P, Medina E, Martín-Zarza P, Fierro JLG (2008) Ti-containing volcanic ash as photocatalyst for degradation of phenol. Energy Environ Sci 1:364–369. https://doi.org/10.1039/B802187M
5. Borges ME, Sierra M, Méndez-Ramos J, Acosta-Mora P, Ruiz-Morales JC, Esparza P (2016) Photocatalysis with solar energy: sunlight-responsive photocatalyst based on TiO_2 loaded on a natural material for wastewater treatment. Sol Energy 135:527–535. https://doi.org/10.1016/j.solmat.2016.06.010
6. Damby DE, Horwell CJ, Baxter PJ, Sparks RSJ, Smith M, Williamson BJ (2014) The respiratory health hazard of tephra from the 2010 Centennial eruption of Merapi with implications for occupational mining of deposits. J Appl Crystallogr 47:1205–1215. https://doi.org/10.1016/j.jvolgeores.2012.09.001
7. de Faria DLA, Venâncio Silva S, de Oliveira MT (1997) Raman microspectroscopy of some iron oxides and oxyhydroxides. J Raman Spectrosc 28:873–878. https://doi.org/10.1002/(SICI)1097-4555(199711)28:11<873::AID-JRS177>3.0.CO;2-B
8. Esparza P, Borges ME, Díaz L, Álvarez-Galván MC, Fierro JLG (2010) Photodegradation of dye pollutants using new nanostructured titania supported on volcanic ashes. Appl Catal A Gen 388:7–14. https://doi.org/10.1016/j.apcata.2010.07.058
9. Faivre D, Frankel RB (2016) Iron oxides: from nature to applications. Wiley-VCH, Weinheim
10. Gardner RFG, Sweett F, Tanner DW (1963) The electrical properties of alpha ferric oxide. J Phys Chem Solids 24:1183–1196. https://doi.org/10.1016/0022-3697(63)90235-X
11. Garibay Febles V, Melo-Máximo DV, Hernández Perez I, Suárez Parra R, Espinoza-Tapia JC, Luna Paz R, Diaz-Barriga Arceo L, Rivera Olvera JN, Melo-Máximo L, González-Reyes L (2022) Synthesis and characterization of α-Fe_2O_3 nanostructured photocatalysts and their application to the degradation of organic pollutants. Crystals 12:1123. https://doi.org/10.3390/cryst12081123
12. Goldstein JI, Newbury DE, Michael JR, Ritchie NWM, Scott JHJ, Joy DC (2018) Scanning electron microscopy and X-ray microanalysis, 4th edn. Springer, New York
13. Guinebretière R (2007) X-ray diffraction by polycrystalline materials. ISTE Ltd, London
14. Hanesch M (2009) Raman spectroscopy of iron oxides and (oxy)hydroxides at low laser power and possible applications in environmental magnetic studies. Geophys J Int 177:941–948. https://doi.org/10.1111/j.1365-246X.2009.04122.x
15. Hernández-Ramírez A, Medina-Ramírez I (eds) (2015) Photocatalytic semiconductors: synthesis, characterization, and environmental applications. Springer, Cham
16. Horwell CJ, Sparks RSJ, Brewer TS, Llewellin EW, Williamson BJ (2003) Characterization of respirable volcanic ash from the Soufrière Hills volcano, Montserrat. Bull Volcanol 65:346–362. https://doi.org/10.1007/s00445-002-0266-6

17. Hu X, Hu X, Peng Q, Zhou L, Tan X, Jiang L, Tang C, Wang H, Liu S, Wang Y, Ning Z (2020) Mechanisms underlying the photocatalytic degradation pathway of ciprofloxacin with heterogeneous TiO_2. Chem Eng J 380:122366. https://doi.org/10.1016/j.cej.2019.122366
18. Jubb AM, Allen HC (2010) Vibrational spectroscopic characterization of hematite, maghemite, and magnetite thin films produced by vapor deposition. ACS Appl Mater Interfaces 2:2804–2812. https://doi.org/10.1021/am1004943
19. Jubu PR, Yam FK, Igba VM, Beh KP (2020) Tauc-plot scale and extrapolation effect on bandgap estimation from UV–Vis–NIR data. J Solid State Chem 290:121576. https://doi.org/10.1016/j.jssc.2020.121576
20. Kubelka P, Munk F (1931) Ein Beitrag zur Optik der Farbanstriche. Z Tech Phys 12:593–601
21. Kümmerer K (2003) Significance of antibiotics in the environment. J Antimicrob Chemother 52:5–7. https://doi.org/10.1093/jac/dkg293
22. Kundu S, Sarkar T, Al-Ahmadi AA, Ali E, Bhattacharjee A (2024) Thermally synthesized hematite (α-Fe_2O_3) nanoparticles as efficient photocatalyst for visible light dye degradation. RSC Adv 14:28944–28955. https://doi.org/10.1039/D4RA04316B
23. Li S, Huang T, Du P, Liu W, Hu J (2020), Photocatalytic transformation fate and toxicity of ciprofloxacin related to dissociation species: Experimental and theoretical evidences. Water Res 185:116286. https://doi.org/10.1016/j.watres.2020.116286
24. Marelli M, Naldoni A, Minguzzi A, Allieta M, Virgili T, Scavia G, Recchia S, Psaro R, Dal Santo V (2014) Hierarchical hematite nanoplatelets for photoelectrochemical water splitting. ACS Appl Mater Interfaces 6:11997–12004. https://doi.org/10.1021/am5030287
25. Martin Del Pozzo AL, González Morán T, Espinosa Pereña R, Butron MA, Reyes M (2008) Characterization of the recent products of Popocatépetl volcano. J Volcanol Geotherm Res 170:61–75. https://doi.org/10.1016/j.jvolgeores.2007.09.004
26. Mishra M, Chun DM (2015) α-Fe_2O_3 as a photocatalytic material: a review. Appl Catal A Gen 498:126–141. https://doi.org/10.1016/j.apcata.2015.03.023
27. Mittal J, Sharma S, Kanchan DK, Verma S, Sharma V, Kumar V, Singh M (2015) Investigation of structural, optical and dielectric properties of cristobalite and quartz. Nucl Instrum Methods B 343:47–53
28. Nidheesh PV (2015) Heterogeneous Fenton catalysts for the abatement of organic pollutants from aqueous solution: a review. RSC Adv 5:40552–40577. https://doi.org/10.1039/C5RA02023A
29. Ocampo-Gaspar M, Cano-Guzmán CF, Payan-Martínez LF, González-Reyes L., Hernández-Pérez I., Garibay-Febles V, Pérez-Orozco JP, Cabrera-Lara LI, Ramón-García ML, Galicia-Luis L, Suárez-Parra R (2018), Sizing the Fenton's catalyst, Journal of Photochemistry and Photobiology A: Chemistry 353, 527-535 https://doi.org/10.1016/j.jphotochem.2017.12.022
30. Orozco SM, Bandala ER, Arancibia-Bulnes CA, Serrano B, Suárez-Parra R, Hernández-Pérez I (2008) Effect of iron salt on the color removal of water containing the azo-dye reactive blue 69 using photo-

assisted Fe(II)/H_2O_2 and Fe(III)/H_2O_2 systems. J Photochem Photobiol A 198:144–149. https://doi.org/10.1016/j.jphotochem.2008.03.001

31. Pignatello JJ, Oliveros E, MacKay A (2006) Advanced oxidation processes for organic contaminant destruction based on the Fenton reaction and related chemistry. Crit Rev Environ Sci Technol 36:1–84. https://doi.org/10.1080/10643380500326564
32. Rajalaxmi M, Rajagopala RJ (2001) Heterogeneous photocatalysis: principles and applications for pollutant degradation. J Chem Technol Biotechnol 76:9–26
33. Ravindran, T.R., Arora, A.K., Ramya, S., Subba Rao, R.V. and Raj, B. (2011), Raman spectroscopic study of medieval Indian art of 17th century. J. Raman Spectrosc., 42: 803-807. https://doi.org/10.1002/jrs.2776
34. Russ JC (1984) Fundamentals of energy dispersive X-ray analysis. Butterworths, London
35. Salma A, Thoröe-Boveleth S, Schmidt TC, Tuerk J (2016) Dependence of transformation product formation on pH during photolytic and photocatalytic degradation of ciprofloxacin. J Hazard Mater 313:49–59. https://doi.org/10.1016/j.jhazmat.2016.03.010
36. Shebanova ON, Lazor P (2003) Raman spectroscopic study of magnetite (Fe_3O_4): a new assignment for the vibrational spectrum. J Raman Spectrosc 34:845–852. https://doi.org/10.1002/jrs.1056
37. Shim SH, Duffy TS (2002) Raman spectroscopy of Fe_2O_3 to 62 GPa. Am Mineral 87:318–326. https://doi.org/10.2138/am-2002-2-314
38. Siebe C, Macías JL (2006) Volcanic hazards in the Mexico City metropolitan area from eruptions at Popocatépetl, Nevado de Toluca, and Jocotitlán stratovolcanoes and monogenetic scoria cones in the Sierra Chichinautzin Volcanic Field. Geol Soc Am Spec Pap 402:253–329. https://doi.org/10.1130/2004.VHITMC.PFG
39. Tamirat AG, Rick J, Dubale AA, Su WN, Hwang BJ (2016) Using hematite for photoelectrochemical water splitting: a review of current progress and challenges. Nanoscale Horiz 1:243–267. https://doi.org/10.1039/C5NH00098J
40. Urban-Chmiel R, Marek A, Stępień-Pyśniak D, Wieczorek K, Dec M, Nowaczek A, Osek J. (2022) Antibiotic Resistance in Bacteria-A Review. Antibiotics (Basel). 2022 Aug 9;11(8):1079. 10.3390/antibiotics11081079

Figures

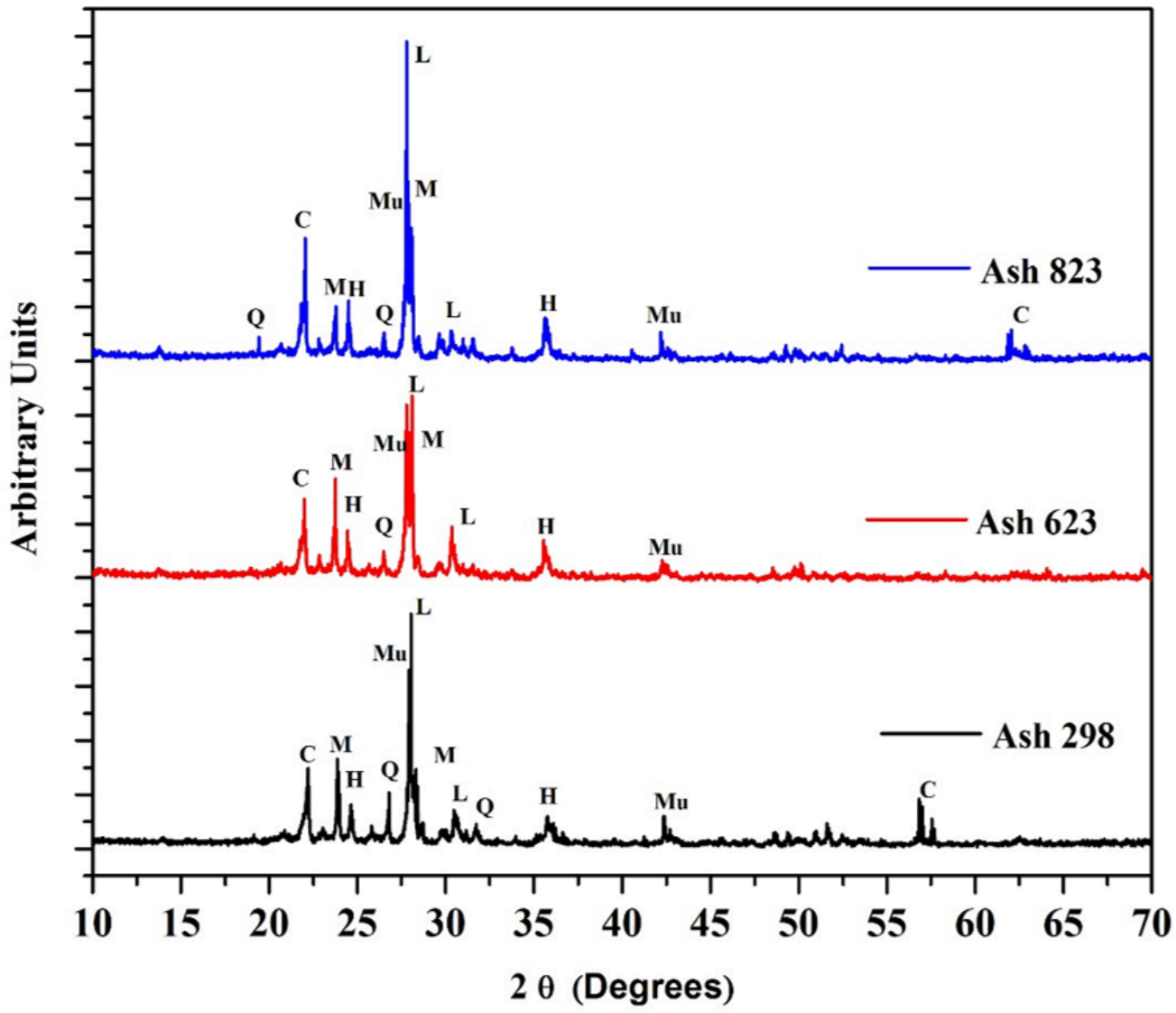


Figure 1

X-ray diffraction patterns of the thermally treated volcanic ash samples (Ash 298, Ash 623, Ash 823). The insets highlight the evolution of the hematite reflections at 2θ ≈ 24.6° (012) and 36.0° (110), which become sharper and more intense with thermal treatment.

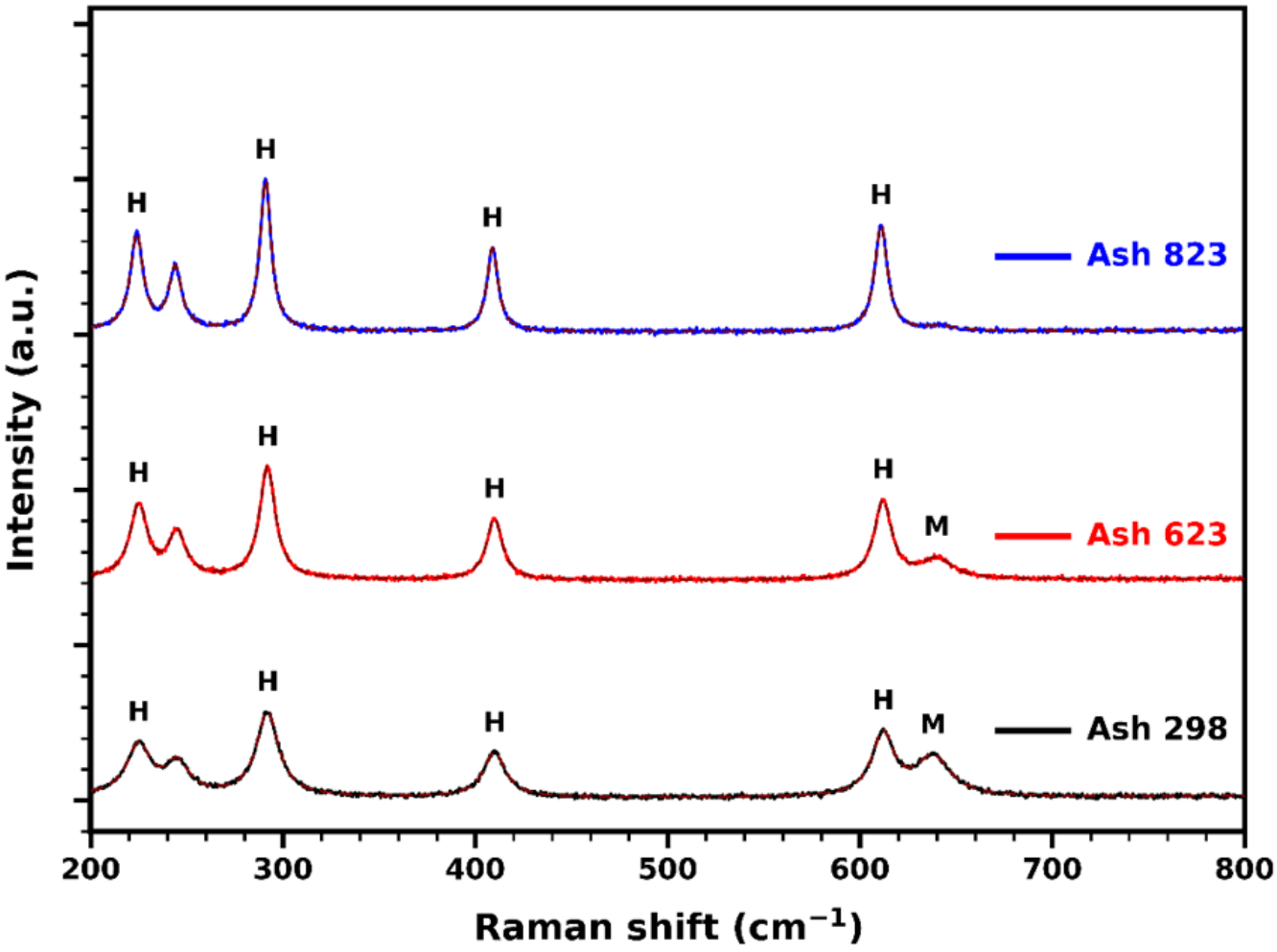


Figure 2

Raman spectra of the volcanic ash samples in the 200–800 cm^{-1} range, after baseline correction. Hematite bands (H) at 225, 245, 292, 410 and 612 cm^{-1} are labeled. The SIBP band at ≈ 640 cm^{-1} (M label in the original figure) decreases progressively with thermal treatment.

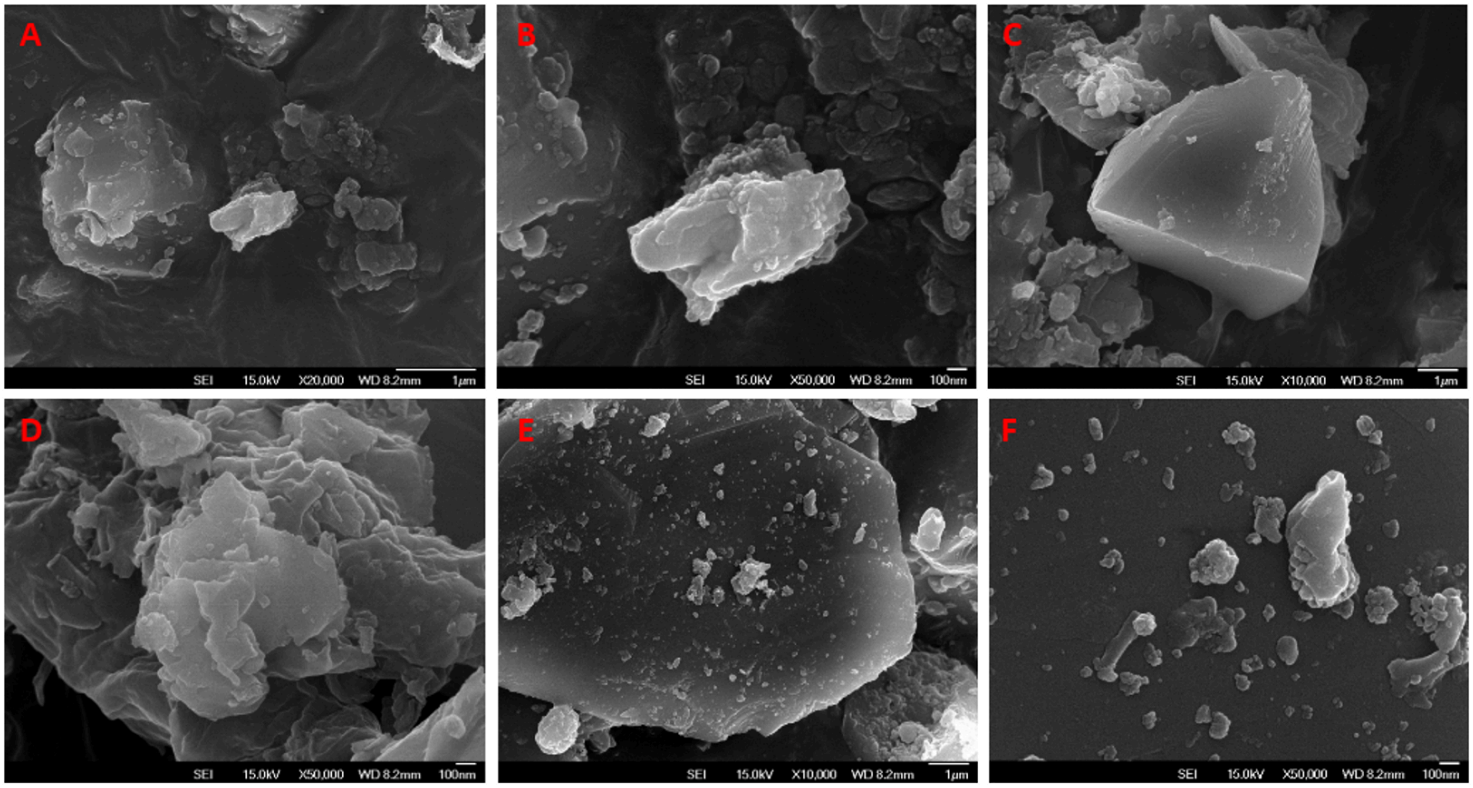


Figure 3

SEM micrographs of the thermally treated volcanic ash samples at two magnifications: (A) Ash 298 ×10,000; (B) Ash 298 ×50,000; (C) Ash 623 ×10,000; (D) Ash 623 ×50,000; (E) Ash 823 ×10,000; (F) Ash 823 ×50,000. Iron-rich particles (bright contrast) are indicated by arrows and decorate the darker silicate matrix.

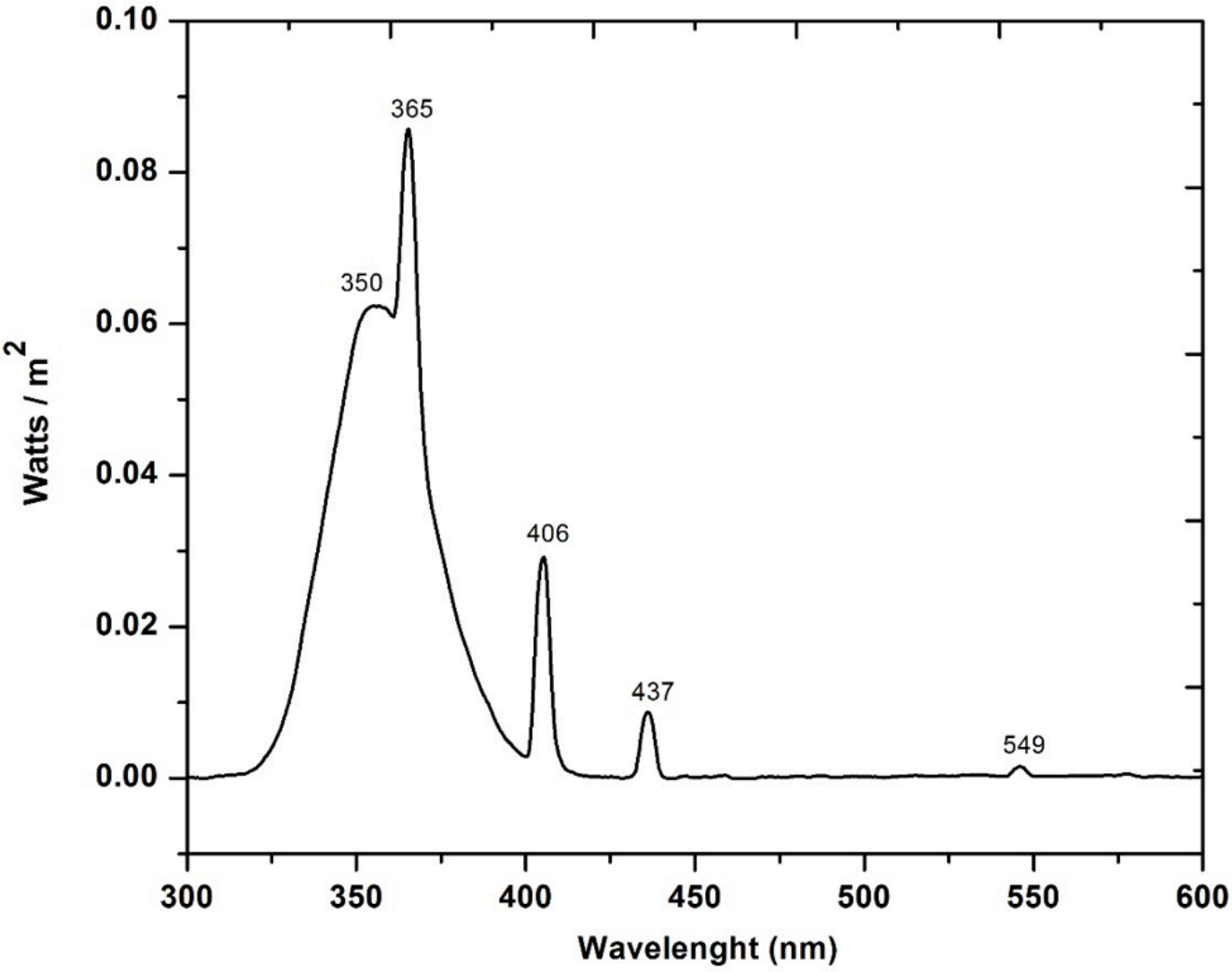


Figure 4

Emission spectrum of the UV lamp (LUMINACTION ES10BLB, 10 W) measured with a StellarNet C-SR-50 spectroradiometer. The main band at 365 nm (and the secondary band at 350 nm, ≈50 % relative intensity) overlaps the absorption onset of the volcanic ash photocatalysts.

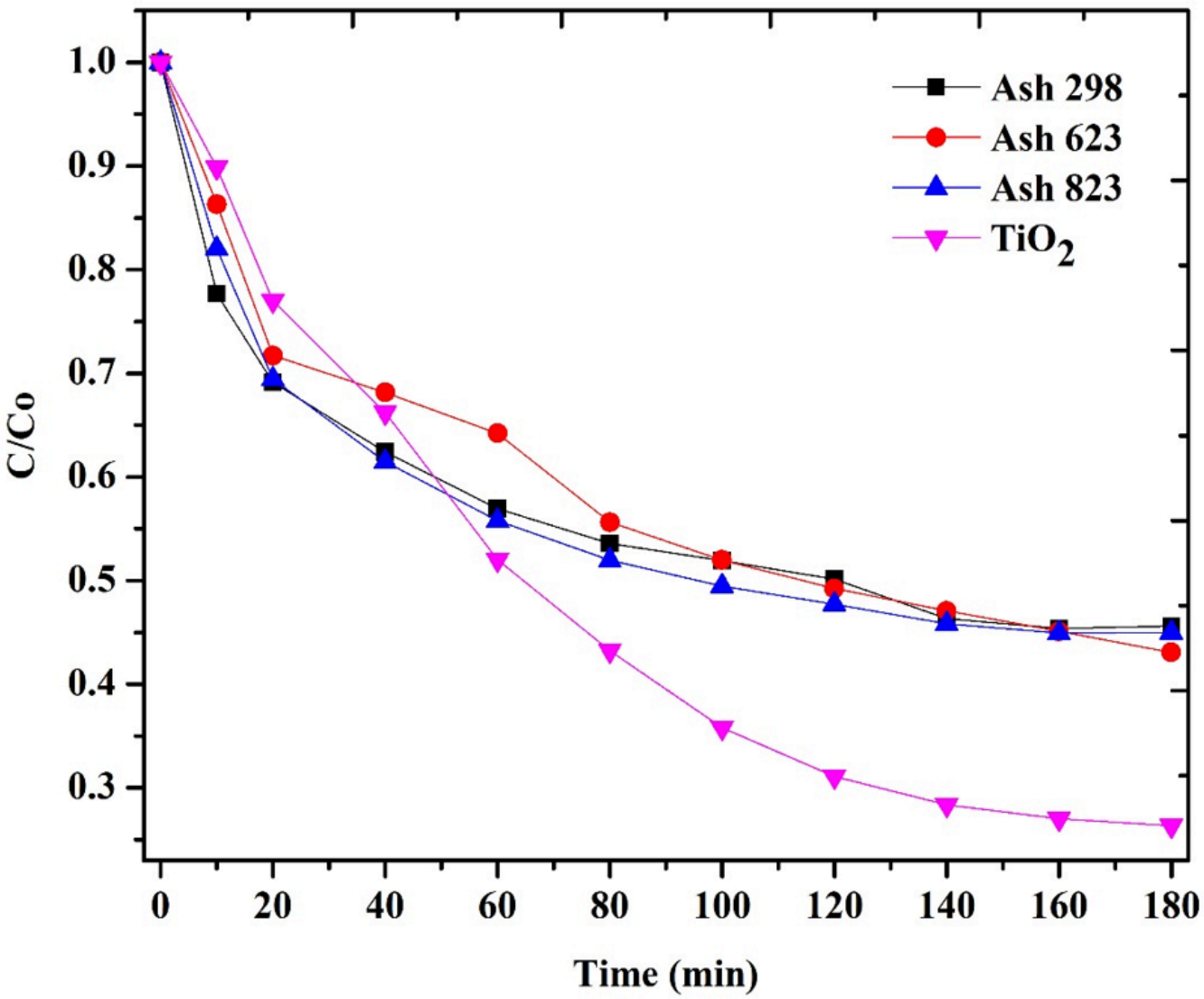


Figure 5

Time-resolved photodegradation profiles of ciprofloxacin (C/C_0 vs. time) under UV-A irradiation in the presence of (■) Ash 298, (●) Ash 623, (▲) Ash 823 and (▼) commercial TiO_2 P25. Reaction conditions: $[CPF]_0$ = 20 mg L^{-1}, catalyst loading 1.25 g L^{-1}, pH 2, 25 °C. Error bars represent the standard deviation of triplicate measurements.

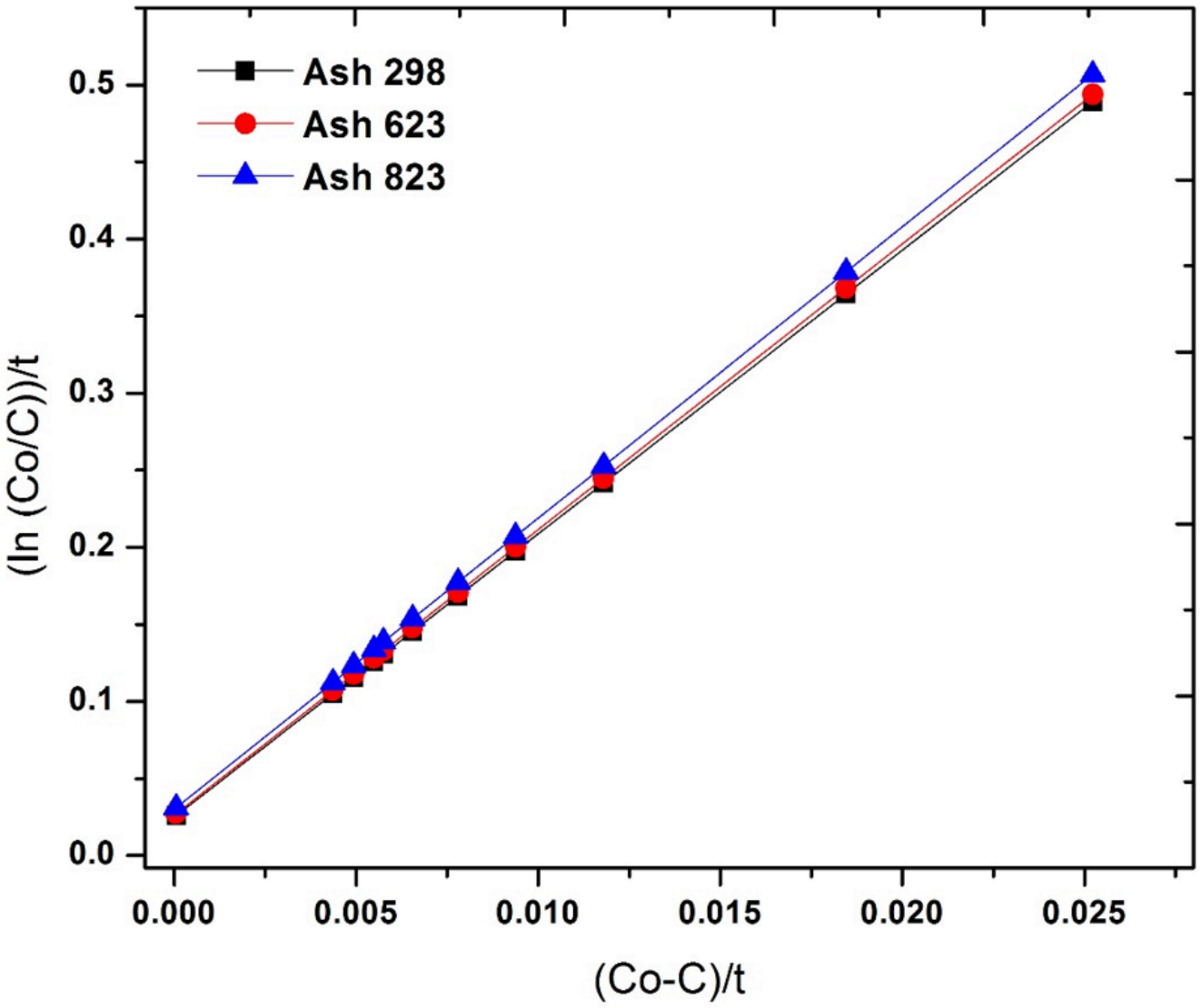


Figure 6

Pseudo-first-order linear fits of $\ln(C_0/C)$ vs. time for the three volcanic ash samples and for TiO_2 P25

Supplementary Files

This is a list of supplementary files associated with this preprint. Click to download.

- GraphicalAbstract.docx